Stratospheric Gravity Wave Fluxes and Scales during DEEPWAVE

RONALD B. SMITH,* ALISON D. NUGENT,* CHRISTOPHER G. KRUSE,* DAVID C. FRITTS,+
JAMES D. DOYLE,# STEVEN D. ECKERMANN,@ MICHAEL J. TAYLOR,& ANDREAS DÖRNBRACK,**
M. UDDSTROM,++ WILLIAM COOPER,## PAVEL ROMASHKIN,## JORGEN JENSEN,## AND STUART BEATON##

* *Department of Geology and Geophysics, Yale University, New Haven, Connecticut*
+ *GATS, Boulder, Colorado*
# *Naval Research Laboratory, Monterey, California*
@ *Naval Research Laboratory, Washington, D.C.*
& *Utah State University, Logan, Utah*
** *German Aerospace Center (DLR), Oberpfaffenhofen, Germany*
++ *National Institute of Water and Atmospheric Research, Kilbirnie, Wellington, New Zealand*
National Center for Atmospheric Research, Boulder, Colorado

(Manuscript received 27 October 2015, in final form 25 February 2016)

ABSTRACT

During the Deep Propagating Gravity Wave Experiment (DEEPWAVE) project in June and July 2014, the Gulfstream V research aircraft flew 97 legs over the Southern Alps of New Zealand and 150 legs over the Tasman Sea and Southern Ocean, mostly in the low stratosphere at 12.1-km altitude. Improved instrument calibration, redundant sensors, longer flight legs, energy flux estimation, and scale analysis revealed several new gravity wave properties. Over the sea, flight-level wave fluxes mostly fell below the detection threshold. Over terrain, disturbances had characteristic mountain wave attributes of positive vertical energy flux (EF_z), negative zonal momentum flux, and upwind horizontal energy flux. In some cases, the fluxes changed rapidly within an 8-h flight, even though environmental conditions were nearly unchanged. The largest observed zonal momentum and vertical energy fluxes were $MF_x = -550$ mPa and $EF_z = 22\,W\,m^{-2}$, respectively.

A wide variety of disturbance scales were found at flight level over New Zealand. The vertical wind variance at flight level was dominated by short "fluxless" waves with wavelengths in the 6–15-km range. Even shorter scales, down to 500 m, were found in wave breaking regions. The wavelength of the flux-carrying mountain waves was much longer—mostly between 60 and 150 km. In the strong cases, however, with $EF_z > 4\,W\,m^{-2}$, the dominant flux wavelength decreased (i.e., "downshifted") to an intermediate wavelength between 20 and 60 km. A potential explanation for the rapid flux changes and the scale "downshifting" is that low-level flow can shift between "terrain following" and "envelope following" associated with trapped air in steep New Zealand valleys.

1. Introduction

Gravity waves are common in Earth's atmosphere as they can be produced by a variety of sources and they are only lightly damped. Their propagation requires that the lapse rate be greater than the dry adiabatic value (i.e., $dT/dz > \Gamma = -g/C_p \approx -9.8°C\,km^{-1}$) and that the intrinsic wave frequency falls in between the buoyancy frequency $N = \sqrt{(g/\theta)(d\theta/dz)}$ and the inertial frequency $f = 2\Omega \sin(\phi)$ (Gossard and Hooke 1975; Gill 1982; Nappo 2012; Sutherland 2010). In these expressions, the symbols g, C_p, θ, Ω, and ϕ are gravity, specific heat capacity, potential temperature, Earth rotation rate, and latitude, respectively. Gravity waves play a significant role in atmospheric dynamics by dispersing mesoscale horizontal potential temperature gradients, aiding geostrophic adjustment, and transporting energy and momentum from source to sink regions (Eliassen and Palm 1960; Bretherton 1969; Holton 1982; Fritts and Nastrom 1992; Alexander et al. 2010).

The current state of knowledge of gravity waves fluxes around the world is nicely reviewed by Geller at al. (2013). They emphasize that satellites and global models are unable to resolve the short wavelength components of the gravity wave spectrum. In addition, wave parameterization schemes are oversimplified and differ from model to model. As a result, there are significant differences and uncertainties in regional wave momentum flux (MF) estimates. In the

Corresponding author address: Ronald B. Smith, Department of Geology and Geophysics, Yale University, P.O. Box 208109, New Haven, CT 06520-8109.
E-mail: ronald.smith@yale.edu

DOI: 10.1175/JAS-D-15-0324.1

Southern Hemisphere winter, for example, the most active wave season and region in the world, zonally averaged MFs estimates at $z = 20$-km range from 2 to 18 mPa.

While satellites, superpressure balloons, and radiosondes provide better spatial and temporal coverage of gravity waves, the most detailed wave observations come from aircraft transects through wave fields, capturing the full spectrum. Physical studies of wave generation and propagation require these targeted high-resolution observations. Furthermore, airborne wave detection has advanced significantly from the 1950s to the present day. Examples of aircraft gravity wave campaigns are given in appendix A.

Early aircraft wave surveys mapped surfaces of constant potential temperature to show airflow ascent and descent. Later surveys combined a gust probe with an inertial platform to deduce three wind components and momentum fluxes. Beginning with T-REX in 2006, GPS altitude measurement allowed detection of static pressure variation and energy flux estimation in mountain waves. The three energy flux components describe the way that gravity waves propagate their energy through the atmosphere.

The recent Deep Propagating Gravity Wave Experiment (DEEPWAVE) campaign (Fritts et al. 2016) was a significant advance over previous gravity wave surveys in many respects. Most importantly, it was the first project to follow waves from the troposphere to the lower thermosphere. This was done by combining flight-level with ground-based, airborne, and satellite remote sensing instruments. Other unique aspects included 1) extensive surveys over land and sea with long legs, 2) targeted observing to improve gravity wave predictions, and 3) better calibrated and redundant in situ airborne sensors. DEEPWAVE is also the first airborne gravity wave project over New Zealand with its isolated rugged terrain and its winter proximity to the Southern Hemisphere polar night jet allowing deep wave propagation. With these advantages, DEEPWAVE seeks new insights into atmospheric gravity wave dynamics and predictability.

The DEEPWAVE project took place in June and July 2014 in the New Zealand region. In this paper, we focus on the flight-level data from the NSF/NCAR Gulfstream V (GV) aircraft. In 26 missions, the GV carried out 97 legs over the Southern Alps of New Zealand and 150 legs over the Tasman Sea and Southern Ocean (Fig. 1). A typical leg length and altitude are 350 and 12.1 km, respectively. Flight-level sampling was done at 1 Hz (240 m) and 25 Hz (10 m). Here we take a statistical approach to this unique dataset. Our statistical results will build a foundation for later case studies, model–data comparisons, and merging flight-level and remote sensing data.

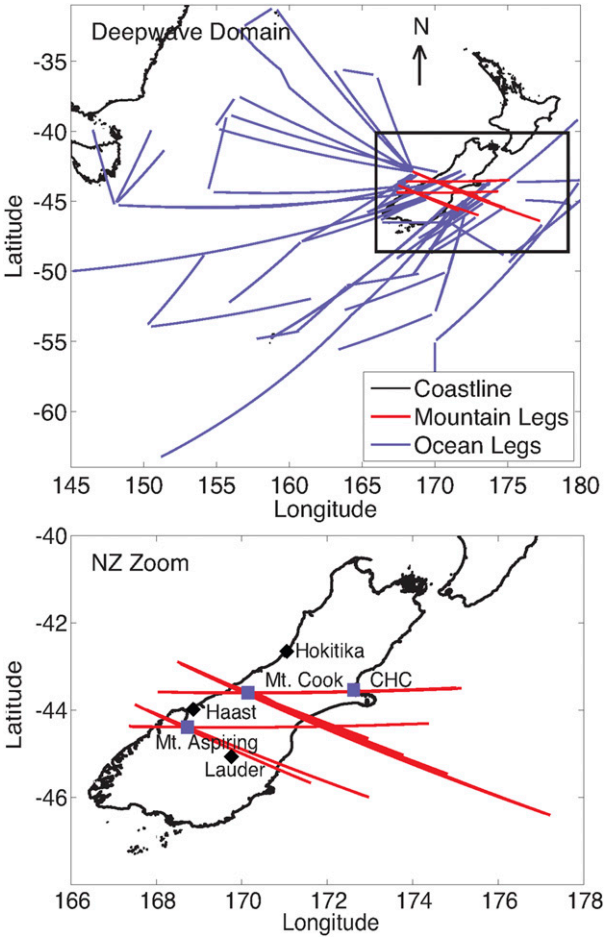

FIG. 1. All DEEPWAVE flight legs during June and July 2014. Most legs were flown at $z = 12.1$ km. (top) Full DEEPWAVE region and (bottom) legs over New Zealand and upper-air stations.

2. Flux calculations

a. *Flux definitions*

In our statistical analysis of flight-level data, we focus on the standard momentum and energy fluxes for nonrotating flow (Eliassen and Palm 1960):

$$\mathrm{MF}_x = \overline{\rho}\,\overline{u'w'}, \tag{1}$$

$$\mathrm{MF}_y = \overline{\rho}\,\overline{v'w'}, \tag{2}$$

$$\mathrm{EF}_z = \overline{P_{cg}w'}, \tag{3}$$

$$\mathrm{EF}_x = \overline{P_{cg}u'}, \tag{4}$$

$$\mathrm{EF}_y = \overline{P_{cg}v'}, \quad \text{and} \tag{5}$$

$$\mathrm{EF}_{zM} = -(\overline{U}\mathrm{MF}_x + \overline{V}\mathrm{MF}_y), \tag{6}$$

where ρ is air density; u', v', and w' are the perturbation zonal, meridional, and vertical wind speeds; P_{cg} is

perturbation pressure corrected for aircraft altitude and cross-track wind; and the overbar indicates spatial leg averages. We computed these six fluxes for all 247 legs from the DEEPWAVE project. A "leg" is defined as a straight and level flight segment usually exceeding 300 km in length. Using the 1-Hz GV data, we subtract the mean values of U, V, W, etc. to obtain the perturbation quantities u', v', and w' and compute variances and fluxes on each leg. There is a slight ambiguity regarding the computation of mean values in choosing between an aircraft mean, a spatial mean, or a parcel weighted mean. This ambiguity changes flux values by no more than 5%. The energy flux [(3)–(5)] estimation is a new capability using corrected static pressure (see below). Equation (6) is the scalar flux with units of vertical energy flux ($\mathrm{W\,m^{-2}}$) formed by the dot product of momentum flux **MF** and the mean horizontal wind **U** vector. In steady small-amplitude waves, it is equal to (3) [see (10) in section 3c].

b. *Correcting the static pressure*

The static pressure recorded in the GV research dataset is measured from a lower fuselage port and corrected for dynamic pressure and angle of attack effects. For use as a dynamically relevant pressure, two other corrections are needed. As the aircraft climbs and descends slightly along a track, we correct the pressure to a constant reference altitude ($\overline{z}$) assuming hydrostatic balance

$$P_C(x) = P(x) + \overline{\rho} g[z(x) - \overline{z}], \tag{7}$$

where z is the aircraft geometric altitude determined from the global positioning system (GPS). As the autopilot is trying to maintain a constant pressure altitude, the variations in P_C along a leg, especially for longer disturbances, come primarily from altitude (z) variations. This kind of correction has been made for several decades over water using a radar altimeter, but only recently could it made over rough terrain using differential GPS (Parish et al. 2007). With estimated OmniStar GPS altitude errors of 10 cm or less, and a typical air density of $0.3\,\mathrm{kg\,m^{-3}}$, the potential error in the second term in (7) is only 0.3 Pa. We have confirmed this altitude accuracy during DEEPWAVE by comparing OmniStar with New Zealand ground GPS stations.

A second source of pressure error is the geostrophic pressure gradient associated with cross-track winds. Whenever the GV flies oblique to the wind vector, a drift in altitude (z) is noted, which from (7) we interpret as the horizontal pressure gradient. Assuming geostrophy, we can compute this pressure trend from the cross-track wind component U_{cross} using

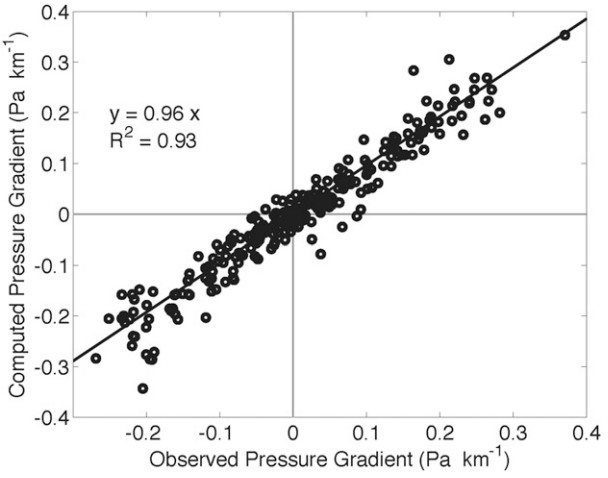

FIG. 2. Observed pressure gradient and computed geostrophic pressure gradient along each leg ($\mathrm{Pa\,km^{-1}}$). Observed primary pressure is corrected for aircraft altitude variation using differential GPS. All DEEPWAVE legs are shown.

$$P_G(x) = 2\overline{\rho}\Omega \sin(\phi) \int_0^x U_{\mathrm{CROSS}}\, dx. \tag{8}$$

Along a 100-km leg, a $5\,\mathrm{m\,s^{-1}}$ crosswind will typically cause [from (8)] $P_G = \pm 30$ Pa. To compare (8) with observations, we compute the average pressure gradient from the regression slope for each leg (Fig. 2). The agreement is excellent showing that both the corrected static pressure and cross-track winds are well determined. The geostrophic pressure gradient is significant when the wind direction and aircraft track heading differ by more than 5°.

As gravity wave propagation is an ageostrophic phenomenon, we subtract the geostrophic pressure gradient to define

$$P_{CG}(x) = P_C(x) - P_G(x). \tag{9}$$

This simple correction significantly improves energy flux calculations and increases its correlation with momentum flux. The T-REX dataset was uncorrected for this effect but the error was minimized by choosing tracks with little crosswind component (Smith et al. 2008). A still simpler approach, used hereafter, is just to detrend the pressure signal before using it for variance or flux calculations.

c. *Measurement uncertainty*

Over the last few years, significant improvements have been made in the calibrations of the NSF/NCAR GV flight-level primary instrument calibrations. These improvements were accomplished in part with the use of a Doppler laser air motion sensor that could detect the aircraft airspeed more accurately than the conventional pitot-static pressure method (Cooper et al. 2014). While this lidar was not used in

TABLE 1. Primary sensor uncertainties on the GV.

Measurement	Units	Bias	Random
Horizontal wind	$m\,s^{-1}$	0.4	0.2
Vertical wind	$m\,s^{-1}$	0.18 (0.05[a])	0.11
Static pressure	Pa	30	10
Temperature	K	0.3	0.1
Geometric altitude	m	0.1	0.1

[a] With latest pitch correction.

DEEPWAVE, the project benefited from these updated calibrations. Our estimated errors for the "primary" sensors are given in Table 1.

From these values, we can estimate the errors that enter the flux calculation. As mean values are removed before flux computation, the flux errors arise only from the random errors. To propagate the errors for momentum flux we imagine a transect with anticorrelated sinusoidal u' and w' oscillations with amplitudes of 5 and $1\,m\,s^{-1}$, respectively. With air density of $0.3\,kg\,m^{-3}$, we define a reference value $MF_x = \rho\langle u'w'\rangle = (0.5)(0.3)(5)(1) = 0.75$ Pa. In a worst-case scenario, the error in Table 1 would translate to a corresponding error in the amplitude of the u' or w' oscillation. In that case, errors in u' and w' will give MF_x errors of $0.2/5 = 4\%$ and $0.11/1 = 11\%$, respectively. If the errors are random and uncorrelated, the MF_x error will be reduced in proportion to the number of samples through the wave. A sampling of $n = 64$ points along the wave will reduce the relative error by the factor $F = n^{-1/2} \sim 0.12$, giving MF_x errors of about 0.5% and 1%, respectively (i.e., 3.75 and 7.5 mPa). The true error probably lies in between these two diverse sets of estimates.

Similar estimates can be done for vertical and horizontal energy flux. Here we neglect errors in geometric altitude and geostrophic pressure. We assume an oscillating pressure (p') with an amplitude of 100 Pa in phase with u' and w' oscillations with amplitudes of 5 and $1\,m\,s^{-1}$ as before. The reference energy flux components are then $EF_x = 250\,W\,m^{-2}$ and $EF_z = 50\,W\,m^{-2}$. In the worst case, the p' and u' errors contribute to EF_x errors of $10/100 = 10\%$ and $0.2/5 = 4\%$, respectively. Errors in p' and w' contribute to EF_z errors of $10/100 = 10\%$ and $0.11/1 = 11\%$. EF_x is slightly more accurate than EF_z. As before, randomness with averaging would reduce these flux errors significantly.

d. Redundant data

Because of the difficulty in translating sensor errors into flux uncertainties, we seek a more robust method to estimate flux errors. A unique aspect of the DEEPWAVE GV flight-level dataset is that several in situ quantities were measured by two independent sensors (Table 2). The sensors believed to be more accurate are called primary. The correlations and linear regression slopes between the primary and secondary sensor pairs are shown in Table 2. The secondary static pressure (PS_A) is an aircraft system signal with some smoothing (Cooper et al. 2014). The wind variables with suffix "_GP" come from the left underwing pod instead of the nose-cone gust probe. The differential GPS altitude GGALT comes from an onboard GPS updated in real time with the OmniStar satellite data. The GGALT_DGPS is corrected after the project using recorded DGPS data from GPS surface stations in New Zealand. A drawback to this "redundancy method" is that the secondary variable will likely dominate the uncertainty and thus overestimate the errors in the primary measurement. Thus, we obtain an upper bound on flux errors.

In Table 2, the regression slope and correlation coefficient between each pair of sensors is shown. Values in the Table 2 are averages over all 247 flight legs. Note that only static pressure and vertical velocity show significant differences. The difference in static pressure arises from the fact that the secondary sensor (PS_A) is part of the GV navigation system and is considerably damped relative to the "research" pressure (PSFX). The impact of these instrument differences on flux calculations is shown in Table 3.

To understand how these sensor differences impact the flux measurements, we exchanged a secondary for a primary sensor and recomputed leg fluxes. An example is shown in Fig. 3, where we replaced the pressure sensor in the EF_z computation. The regression slope is 0.85, less than unity, owing to the damping on the secondary pressure. The scatter suggests an EF_z uncertainty of at least $1\,W\,m^{-2}$. In Table 3, we show the difference in all

TABLE 2. Redundant variables from the GV in DEEPWAVE.

Physical quantity	Primary	Secondary	CC	Slope	Flights with secondary sensor
Static pressure	PSXF	PS_A	0.7	0.6	All
Vertical wind	WIC	WI_GP	0.95	0.95	Most
Horizontal wind; eastward	UIC	U_GP	0.97	0.95	Most
Horizontal wind; northward	VIC	VI_GP	0.97	1.0	Most
Air temperature	ATX	ATHR1	0.995	1.0	All
Geometric altitude	GGALT OmniStar	GGALT_DGPS	0.993	1.0	Several

TABLE 3. Redundant leg-average flux measurements (all flights). The asterisk indicates bad data owing to outliers.

Quantity	Pair	R squared	Slope	MAE	Target	%
$MF_x = \langle w', u' \rangle$	PS/SP	0.51/0.97	0.88/0.998	0.035/0.0061	0.1	36/6
$MF_y = \langle w', v' \rangle$	PS/SP	*/0.99	*/1.01	0.049/0.0087	0.1	45/9
$EF_x = \langle p', u' \rangle$	PS/SP	0.98/0.96	1.01/1.01	2.12/1.89	40	5/5
$EF_y = \langle p', v' \rangle$	PS/SP	0.99/0.98	1.01/0.97	1.80/2.43	40	5/6
$EF_z = \langle p', w' \rangle$	PS/SP	0.87/0.91	0.85/0.84	0.387/0.415	5	8/8

the leg flux estimates caused by swapping a secondary for a primary sensor. In the "pair" column, PS/SP gives the order that w' and u' are taken from the primary (P) and secondary (S) sensors. To describe how these redundant measurements compare, we show the R squared and slope of the regression line and the mean absolute error (MAE). Each flux involves two sensors and both swaps are considered: PS and SP. All 247 legs are included. The last two columns give a target flux value that we would expect to find and measure over mountains and the expected relative errors using the MAE values, respectively. For example, our target zonal momentum flux is $MF_x = 0.1\,\text{Pa} = 100\,\text{mPa}$ and target vertical energy flux is $5\,\text{W m}^{-2}$. Errors in the secondary w sensor degrade the MF_x and EF_z estimates. The actual errors in the primary sensors may be much smaller than given in Table 3.

In general, we see good agreement between the different estimates of these fluxes. The best accuracy is for the horizontal energy flux (EF_x, EF_y) with differences less than 5%. While this quantity has not been computed from flight data before, we conclude that it can be robustly estimated. It gives valuable information about how the wave is propagating horizontally through the atmosphere. Note that these error estimates do not include sampling errors. Even in simple mountain wave fields, fluxes are inhomogeneous (Vosper and Mobbs 1998; Kruse and Smith 2015) and a single aircraft traverse is unlikely to give a spatially and temporally representative flux value.

3. Flux results

a. Land versus sea

The extensive over-ocean surveys in DEEPWAVE allow us to compare stratospheric waves over mountainous terrain with those over the sea using the same platform and instruments. Is there a significant difference between land and sea gravity waves? Are the waves over the sea in excess of our threshold detection level? Figure 4 shows EF_z plotted against the distance between the leg center and a Mt. Cook reference point (43.60°S, 170.14°E). Legs with distances greater than 300 km are primarily ocean legs but may include a few transects over remote islands. The EF_z values for distant legs have random sign and seldom exceed $1\,\text{W m}^{-2}$ in magnitude—our rough detection threshold. The cluster at 1460 km is from Macquarie Island—RF23. The large flux at 1930 km

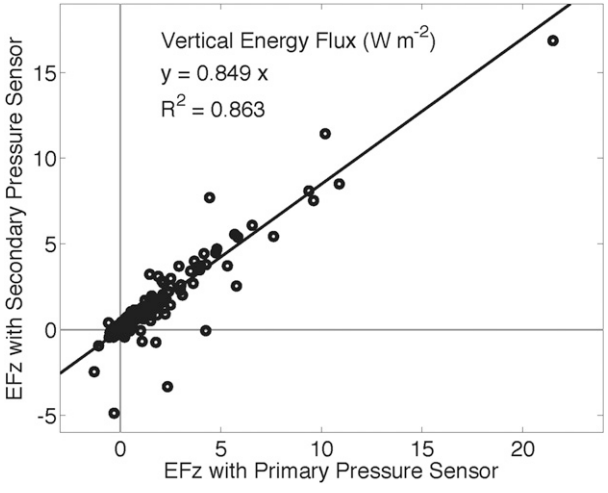

FIG. 3. EF_z (W m^{-2}) using the primary and secondary static pressure sensors while maintaining the primary vertical velocity sensor. Many such diagrams are summarized in Table 3.

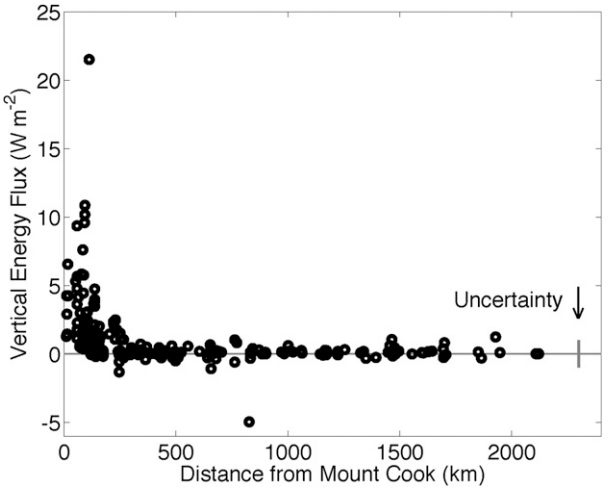

FIG. 4. EF_z (W m^{-2}) for all 243 DEEPWAVE legs vs distance from Mt. Cook. Distances greater than 300 km are over the sea or some oceanic island. A reference flux uncertainty value is shown.

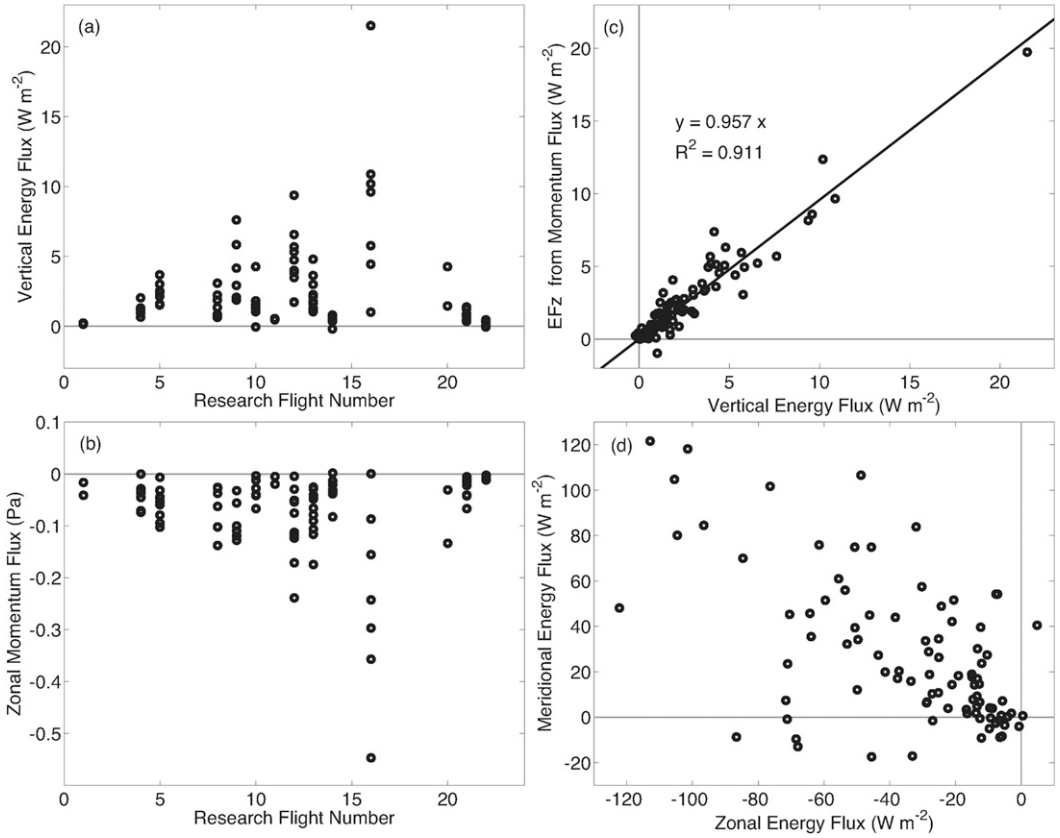

FIG. 5. Energy and momentum fluxes from DEEPWAVE flights over New Zealand. (a) Vertical energy flux vs flight number, (b) zonal momentum flux vs flight number, (c) vertical energy flux vs scalar momentum flux, and (d) vector horizontal energy flux.

is from Tasmania—RF06. The largest outlier, the negative value $EF_z = -5\,W\,m^{-2}$ at 800 km, is a large-scale wave not properly sampled by the GV. For the remainder of this study we focus on the 14 New Zealand flights with legs over the mountainous Southern Alps terrain (Fig. 1b).

b. Momentum and energy fluxes over New Zealand

The energy and momentum fluxes for all 14 New Zealand flights are shown in Fig. 5. In Fig. 5a, the leg EF_z magnitudes vary widely between and within flights, but all EF_z values are positive, indicating upward propagating waves. In flights RF2, -11, -14, and -22, the fluxes are very small—less than $1\,W\,m^{-2}$. In four flights—RF9, -12, -13, and -16—leg values of EF_z exceeded $5\,W\,m^{-2}$. The strongest fluxes were found in RF16 leg 1 with $MF_x = -550$ mPa and $EF_z = 22\,W\,m^{-2}$.

The zonal momentum fluxes (MF_x) shown in Fig. 5b show a similar pattern of weak and strong flights and legs. All MF_x values are negative as expected for steady mountain waves in westerly ambient airflow. In selecting New Zealand flights for this section, we have removed RF26 owing to its unusual ridge-parallel leg orientation.

c. Relationship between momentum and energy flux

According to Eliassen and Palm (1960), there is a simple relationship between energy and momentum flux for linear, steady nondissipating mountain waves:

$$EF_z = -\mathbf{U}\cdot\mathbf{MF} = EF_{zM}. \tag{10}$$

While (10) is rather general, it can be understood in simple cases as arising from the inverse relationship between perturbation pressure and velocity in the linearized horizontal momentum equation (e.g., $\overline{\rho}\,\overline{U}u' = -p'$). To test (10) against our New Zealand data, we plot leg-averaged EF_z [(3)] versus EF_{zM} [(6)] in Fig. 5c.

The agreement between the energy and momentum flux is excellent, suggesting that our measurements are good and the assumptions behind (10) are valid. Both the slope and *R*-squared values are near unity. The scatter suggests a random error in EF_z and/or EF_{zM} of about $1\,W\,m^{-2}$. A similar test was performed for T-REX

data (Smith et al. 2008) with good agreement (slope = 0.86), but not as good as found here (slope = 0.96). The marked improvement in the current case appears to be due to improved data quality and the geostrophic correction (i.e., detrending) to the pressure field.

d. Horizontal energy flux

According to linear wave theory, vertically propagating mountain waves must have a horizontal component to their energy flux. They propagate upwind through the air in order to balance the strong downwind advection of wave energy by the mean flow. As indicated in section 2, we are able to compute EF_x [(4)] and EF_y [(5)] with considerable accuracy. The horizontal EF vectors are shown in Fig. 5d for all the New Zealand mountain legs. With only one exception, the energy propagation is westward or northwestward, opposing the mean winds and roughly perpendicular to the ridge crest. This adds certainty to our interpretation of the disturbances over New Zealand as mountain waves.

Typically, the horizontal energy fluxes [(4) and (5)] over New Zealand are a factor of 15 or so larger than the vertical energy flux [(3)]. A typical value is $EF_x = -60\,W\,m^{-2}$, while $EF_z = 4\,W\,m^{-2}$. In simple environments, the ratio $R = EF_z/EF_x \approx 1/15$ represents the slope of the phase lines, the slope of the gravity wave ray path relative to the fluid, and the ratio of the vertical to horizontal wavelength.

e. Flux variation and low-level winds

According to classical linear mountain wave theory, the mountain wave fluxes increase systematically with increased wind speed U across the mountain. In unsheared hydrostatic flow (e.g., Queney 1948), for example,

$$\text{Wave Drag} = C_D \rho N U h^2 \quad \text{and} \tag{11a}$$

$$\text{Wave Energy Generation} = C_D \rho N U^2 h^2 \tag{11b}$$

(appendix B). The control of energy flux by wind speed is tested in Fig. 6, where we plot aircraft observed EF_z at 12.1 km versus the low-level ($z = 4$ km) wind speed across the terrain directly underneath the aircraft. A similar plot can be made for MF_x. The low-level wind speed is determined from a nested 6-km WRF simulation with ECMWF analysis boundary conditions, as described by Kruse and Smith (2015). This is the perhaps best available estimate of the winds across the terrain directly underneath the aircraft. Our DEEPWAVE results seem to violate simple wind speed control. The figure shows no one-to-one relationship between wind speed and flux. At wind speeds above $20\,m\,s^{-1}$, the energy and momentum fluxes fluctuate between large and small values. Perhaps it is only the upper value that is controlled by the wind speed. This result supports the idea of some instability in the wave generation process. One possibility is the resonant reflection from wave breaking aloft (e.g., Smith 1985). Another possible cause is discussed in section 9 is related to how the airflow follows the complex terrain. A similar comparison was done by Lilly et al. (1982) for the front range and Smith et al. (2008) with little evidence for such unsteadiness.

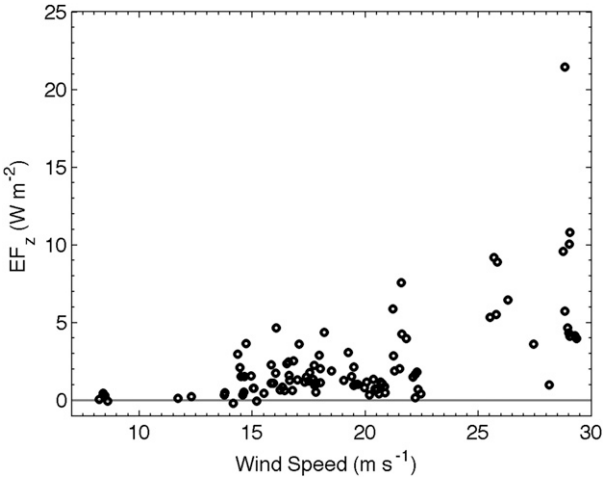

FIG. 6. Leg-averaged EF_z for all 93 New Zealand legs vs model-derived wind speed under the aircraft at $z = 4$ km. The wind speed may set an upper bound on EF_z, but not the value itself.

Another approach to understanding the flux magnitude is to examine the fluxes on subsequent cross-mountain legs to reveal any rapid changes. A typical elapsed time between legs is about 45 min. The most striking example of flux unsteadiness is the strongest event: RF16 on 4 July 2014. In Fig. 7 (see also Figs. 5a,b), we show that the energy flux drops from 22 to $0\,W\,m^{-2}$ during sequential legs 1–4 and recovers on later legs 8–9, all at 12.1 km. The zonal momentum flux shows a corresponding fluctuation. During these fluctuations, the low-level wind speed was nearly constant at $U = 29\,m\,s^{-1}$ (Fig. 7). The flight-level winds decreased slowly. Leg 5, flown higher, illustrates the negative vertical wind shear not temporal change.

4. Atmospheric profiles over New Zealand

The environments in which the waves propagate over New Zealand were well observed in DEEPWAVE using frequent radiosondes from Hokitika, Lauder, and Haast (Fig. 1b). Profiles from GV dropsondes and inversion of radiances from the airborne microwave temperature profiler (MTP) are also available from all flights. Sample radiosonde profiles for 29 June (RF12) and 4 July (RF16) are shown in Fig. 8. The profiles agree at larger

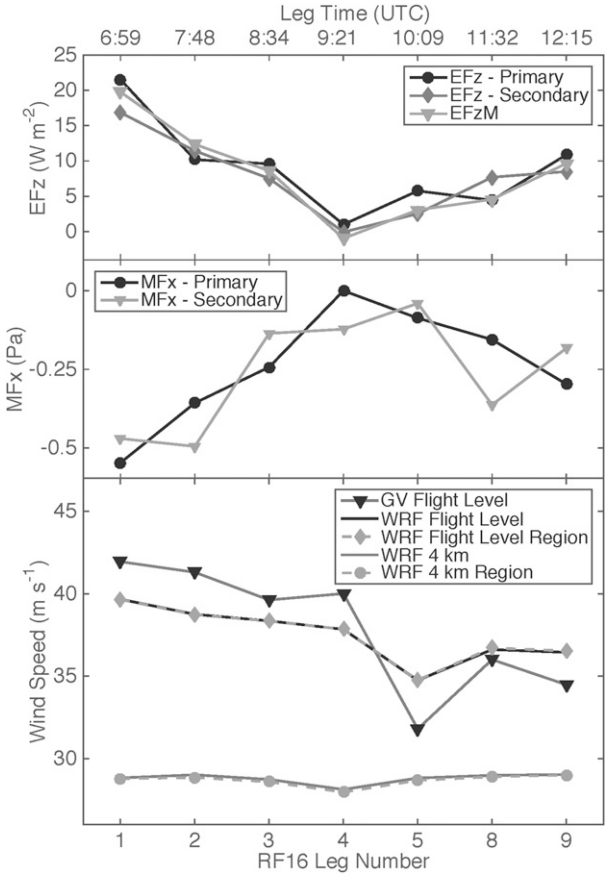

FIG. 7. Fluxes and winds during the strongest DEEPWAVE event (RF16 on 4 Jul 2014). (top) Three redundant estimates of vertical energy flux (EF_z). (middle) Two redundant measurements of zonal momentum flux (MF_x). (bottom) Mean winds at 4 km and at flight level. Seven cross-mountain legs (1–5, 8–9) over Mt. Aspiring are shown with leg times (UTC). The elapsed time between legs is about 45 min. All legs were flown at 12.1 km except leg 5 at 13 km.

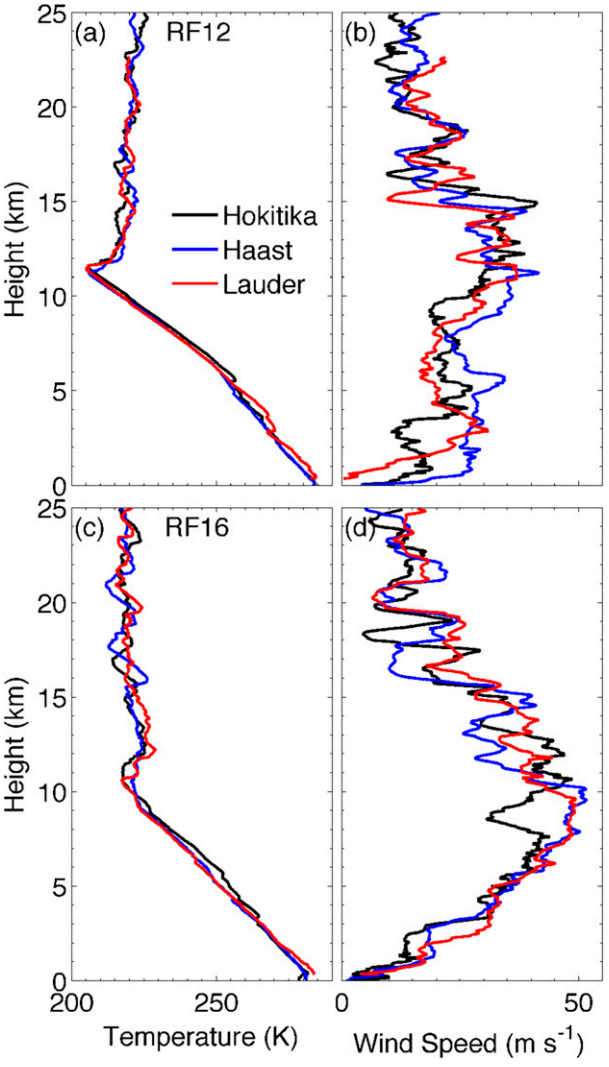

FIG. 8. Balloon soundings at 0900 UTC from Hokitika, Haast, and Lauder: (a),(b) 29 Jun 2015 for RF12 and (c),(d) 4 Jul 2015 for RF16. Note the tropopause inversion layer and wave-induced oscillations.

vertical scales but show uncorrelated oscillations caused by mountain waves. A striking aspect of both soundings is the tropopause inversion layer [TIL; see Birner (2006) and Gettelman and Wang (2015)]. The aircraft at z = 12.1 km is generally flying within or just above the TIL. As the wind speeds are relatively high at this altitude, the waves are more ''linear'' than they are at other altitudes (Kruse and Smith 2015). The profiles in Fig. 8 are useful in interpreting the flight-level data shown in the sections below.

5. Vertical displacement patterns

A useful way to visualize mountain wave patterns is to compute the vertical displacement of air parcels as they cross the mountain range. Assuming that the wave field is steady and the wind is along the flight track and that the displacements are small, we use the flight-level winds to compute the kinematic displacement

$$d(x) = \int_0^x \left(\frac{w'}{U}\right) dx. \tag{12}$$

In (12), we use the perturbation vertical velocity $w'(x)$ and total along-track wind speed $U(x)$ (Smith et al. 2008). The mean vertical velocity has been subtracted from each leg according to $w' = w - \overline{w}$. The integral begins at the upwind end of the cross-mountain leg. The $d(x)$ patterns for RF12 and RF16 are shown in Fig. 9 for all cross-mountain legs. These traces show the smooth upwind region, the waves over the mountain crest, and

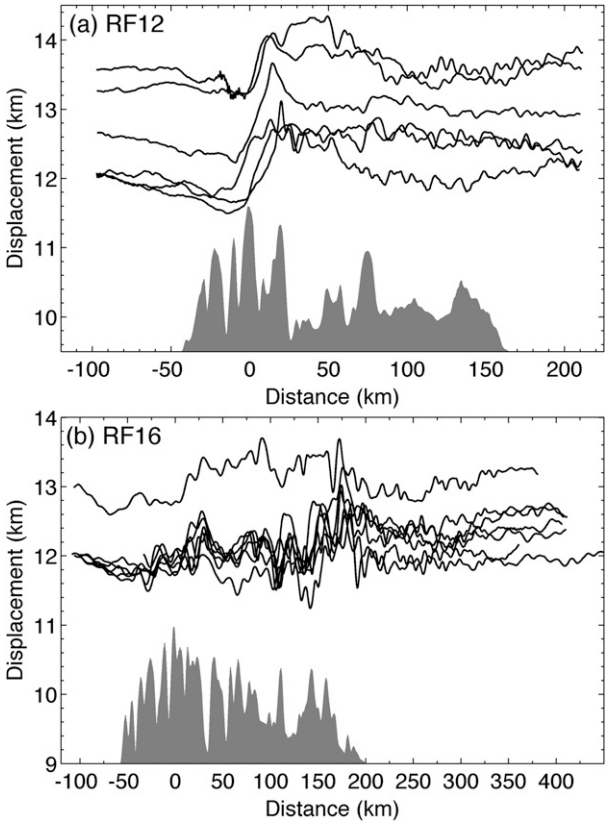

FIG. 9. Vertical air parcel displacement [(11)] for legs over Mt. Aspiring from flights (a) RF12 and (b) RF16. The terrain is shown with proper vertical scale but lifted.

the short periodic waves downwind. The bottom panel in Fig. 9 shows the extreme ruggedness of the New Zealand terrain.

The reader's eye may at first fail to distinguish between the weaker RF12 event and stronger RF16 event or between the weak and strong legs on RF16 (Figs. 5a, b). The significant differences between these legs are masked by the dominance of energetic short waves with a horizontal wavelength of about 10 km. As we will see in section 6, these short waves carry little vertical energy and momentum flux and so are "fluxless." It is the longer waves hidden within these short waves that carry the fluxes. This confusion motivates the scale analysis in the next section.

6. Scale analysis

The cross-island transects of air motion, temperature, and pressure contain a wide variety of scales—from a few tens of meters to 300 km. The interpretation of these different scales poses a challenge for the analyst. An important characteristic of a wave field is the dominant wavelength(s) of the flux-carrying wave(s). Additionally, there may be other disturbance scales that do not carry fluxes. To guide our discussion of scale, we introduce a scale terminology in Table 4. The acronym "LIST" helps one to remember these scale categories. The long wave category is limited by the typical aircraft leg length of 350 km. The turbulence category is limited by the 25-Hz sampling interval of about 10 m.

With only a few exceptions, the waves carrying upward energy flux and downward momentum flux over New Zealand lie in the ranges of wavelengths between 20 and 150 km. For discussion purposes, we arbitrarily divide this range at 60 km into long and intermediate waves (Table 4). Examples of long (RF12) and intermediate (RF16) wave cases are given in Figs. 10 and 11 and Figs. 12 and 13, respectively. These figures include a cross-mountain transect of flight-level variables and wavelet and spectral analyses of vertical motion and vertical energy flux. Both flight legs are over rugged Mt. Aspiring for easy comparison.

a. *Case RF12, leg 10*

Research flight RF12 occurred on 29 June 2014 with moderate wind across the Southern Alps (Figs. 8b and 9a). The flight-level data for leg 10 is shown in Fig. 10. In Fig. 10e, the accumulative EF_z is shown, normalized by the total leg length. The wavelet and power spectral analyses for $w(x)$ variance and $EF_z = p'w'$ are shown in Fig. 11. The variance wavelet for w' and covariance wavelets for $p'w'$ are computed using the method of Woods and Smith (2010). Figures 10 and 11 show that the w variance is dominated by short waves with $\lambda \approx 8$ km with smaller peaks at intermediate (40 km) and long (80 km) wavelengths. The energy flux is dominated by waves in the long category with $\lambda \approx 80$ km. The short waves make no contribution to EF_z. The short waves are distributed in bursts over the broad Mt. Aspiring massif while the flux-carrying long waves are concentrated over the western edge.

b. *Case RF16, leg 1*

Research flight RF16 occurred on 4 July 2014 with strong wind across the Southern Alps (Figs. 8d and 9b). Leg 1 on this day carried the largest fluxes in the entire DEEPWAVE project ($MF_x = -300$ mPa, $EF_z = 22\,W\,m^{-2}$). The transect data for leg 1 is shown in Fig. 12. The wavelet and power spectral analyses for $w(x)$ variance and $EF_z = p'w'$ are shown in Fig. 13. Figure 13 shows that the w variance is dominated by short waves with $\lambda \approx 11$ km with a nearly equal peak at 30 km. The energy flux is dominated by waves in the intermediate category with $\lambda \approx 30$ km . Again, the short waves make no contribution to EF_z. The short waves are

TABLE 4. Wavelength categories for DEEPWAVE flight-level signals.

Term	Code	Wavelength (km)	Occurrence and interpretation
Long	L	60–150	Flux-carrying mountain waves Propagate upwind
Intermediate	I	20–60	Flux-carrying mountain waves Dominate strong cases Propagate upwind
Short	S	6–20	Dominate w power Usually fluxless Propagate upwind
Turbulence	T	0.1–2	Rare, strong w power, no energy flux

distributed in bursts over the broad Aspiring Massif while the flux-carrying intermediate waves are concentrated over the eastern edge.

Occasionally, hints of flux-carrying waves longer than 150 km are seen in DEEPWAVE New Zealand legs. We ignore these here for three reasons: they contribute little to the total flux, they are barely captured in the 300-km cross-mountain legs, and their intrinsic frequency would be comparable to the Coriolis force time scale of 3 h at 44°S latitude.

c. *Spatial filter analysis*

While spectral and wavelet analyses (Figs. 11 and 13) are useful for leg-by-leg scale analysis, it is not possible to show such diagrams for all 97 New Zealand legs. Instead, we turn to high- and low-pass spatial filters for a statistical-scale analysis of all the New Zealand DEEPWAVE legs. Here we use a triangle (i.e., ''double boxcar'') low-pass filter which attenuates the shorter waves according to

$$F_{\rm LP}(\lambda) = \mathrm{sinc}^2(D/\lambda), \tag{13}$$

where λ is the wavelength, D is the width of the boxcar, and $\mathrm{sinc}(D/\lambda) = \sin[\pi(D/\lambda)]/[\pi(D/\lambda)]$. The corresponding high-pass filter $F_{\rm HP}(\lambda) = 1 - F_{\rm LP}(\lambda)$ attenuates the longer waves. The cross-over wavelength λ_C, where $F_{\rm LP} = F_{\rm HP} = \frac{1}{2}$, occurs at about $\lambda_C = 2.2D$. Choosing various D values allows the filter to separate the wave categories in Table 4. To start, we show the results for a boxcar width of $N = 45$ points giving $D = 10.8$ km so the cross-over wavelength for (13) is $\lambda_C = 24$ km (Fig. 14). This high-pass filter captures the short waves with little contamination from the intermediate waves. The low-pass filter captures the long waves with some contribution from the intermediate waves.

Figure 14 shows the variances for high- and low-passed vertical winds (w'). The regression line slopes indicate the fraction of the signal that survives the filter. The w-variance signal comes through the high-pass filter ($\lambda_C < 24$ km) nearly untouched (83%) while the low-pass filter cuts the variance to 37%, implying that $F_{\rm LP} \approx \sqrt{0.37} = 0.61$ so the dominant wavelength [(13)] is about $\lambda \approx (0.35)(24) = 8$ km. Our interpretation of this striking difference in filter response is that the vertical winds are dominantly short. While vertical winds are essential for vertical fluxes, they are dominated by short fluxless waves. This result was seen in Figs. 11 and 13 and is amplified below.

Figures 15a and 15b show the pressure–velocity correlations for the low- and high-pass waves. We use the normalized correlation coefficient (CC) with generic signals $f(x)$ and $g(x)$,

$$\mathrm{CC}(f,g) = \overline{f'g'}/[\overline{f'f'}\,\overline{g'g'}]^{1/2}, \tag{14}$$

to show the tendency of these waves to propagate vertically and horizontally, independent of their amplitude:

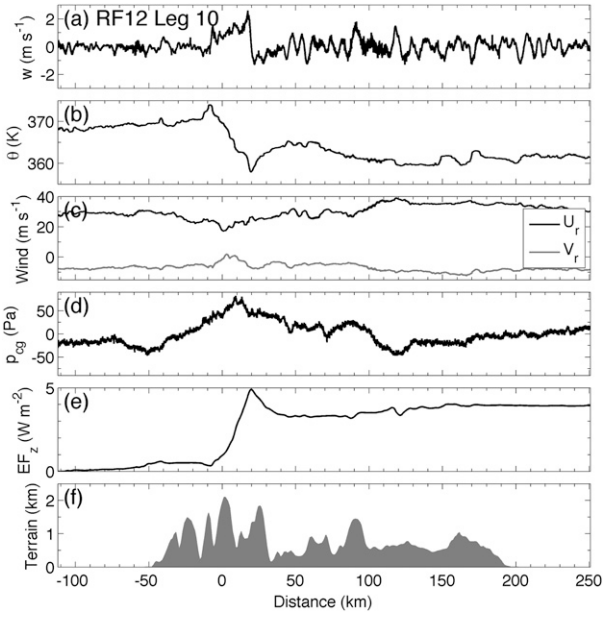

FIG. 10. GV flight-level data from the RF12 leg 10 transect: (a) vertical velocity, (b) potential temperature, (c) cross-track and along-track winds, (d) corrected pressure (P_{cg}), (e) running sum of EF_z, and (f) terrain.

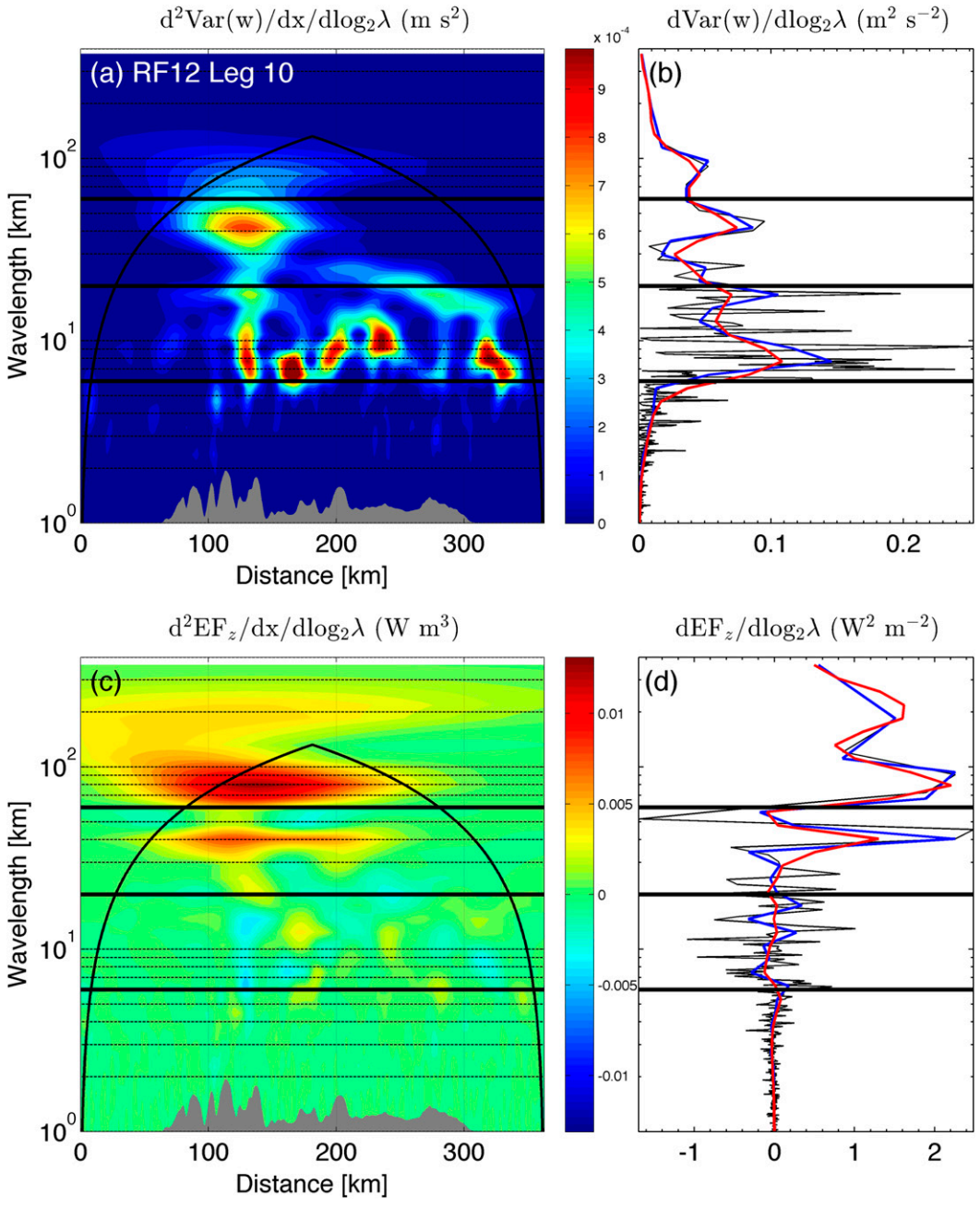

FIG. 11. Scale analysis for RF12 leg 10: (a) w-power wavelet, (b) w-power spectrum, (c) EF_z wavelet, and (d) EF_z spectrum. The spectra show three estimates: raw (black), smoothed (blue), and integrated wavelet (red). Thick reference lines divide long, intermediate, and short waves (Table 4).

the higher the CC, the more these signals resemble propagating gravity waves. The low-pass (i.e., long and intermediate) waves have positive CC(p', w') and negative CC(p', u'), indicating upward and westward propagation. The high-pass (i.e., short) waves have near-zero CC(p', w') and negative CC(p', u'), indicating westward but no vertical propagation. We conclude that the longer waves carry momentum and energy vertically and have the mountain wave signature of upwind propagation. The short waves appear to propagate upwind too, but not vertically.

These attributes of the short waves are analogous to ducted or trapped lee waves often seen in the lower troposphere (e.g., Scorer 1949; Smith 1976). One possibility is that the tropopause inversion layer (section 4) acts as a wave duct. If they are not vertically propagating

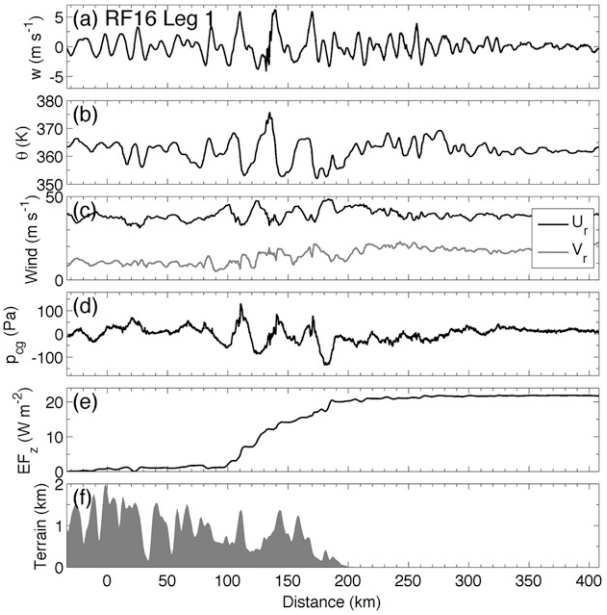

FIG. 12. As in Fig. 10, but for the extreme case of RF16 leg 1 with $EF_z = 22\,W\,m^{-2}$.

waves, they may have been generated at their observed altitude by a nonlinear mechanism. Short waves may also be "leaky" or weakly evanescent waves with wavenumbers near the Scorer parameter. These Short waves are absent over the sea, except downwind of New Zealand, confirming that they are mountain induced, not some ambient background signal or an artifact of the aircraft measurements.

The possibility that short waves may be an artifact of observing error has been raised by Zhang et al. (2015). They worry that the aircraft rises and falls in response to these vertical air motions, moving it off from a constant pressure surface. In fact, as long as the aircraft inertial platform, gust probe, and GPS systems are functioning properly, as we believe they were, (7) and the other corrections should remove such influences of aircraft motion.

To further verify the existence of the short wave bursts, we applied the $N = 45$ ($D = 10.8$ km, $\lambda_C = 24$ km) high-pass filter to the primary (i.e., nose cone) and secondary (i.e., left wing pod) gust probes. This filter will isolate the short waves. These two gust-probe systems have independent differential pressure ports and inertial platforms. The resultant w variances correlated almost perfectly (i.e., slope = 1.009 and R squared = 0.9986) from leg to leg. This dataset includes legs flown along and against the wind, between which the aircraft altitude phase response varies. The agreement between these two independent instruments supports the existence of the short waves.

In Fig. 16, we use a wider filter with $N = 120$, $D = 28.8$ km to separate the long (i.e., low pass) from intermediate (i.e., high pass) waves from all the New Zealand legs. The cross-over wavelength is $\lambda_C = 63$ km—near the boundary between long and intermediate waves (Table 4). In this diagram we show the ratio of the partial EF_z to the total EF_z as a function of the total EF_z. In the legs with weaker fluxes, the low-pass (i.e., long) waves slightly dominate the EF_z but the strongest flux legs (with $EF_z > 4\,W\,m^{-2}$) are clearly dominated by the high-pass (i.e., intermediate) waves. This is a remarkable result, suggesting that in the strong flux events, the mountain waves "downshift" to use intermediate wavelengths. The results from cases RF12 and RF16, shown earlier, support this finding.

7. Wave-induced turbulence

On four occasions during RF09 and RF12, by climbing above 13 km, the GV aircraft was able to enter the zone of mountain wave breaking. On three other occasions (RF03, -13, -21), weaker turbulent zones were identified at $z = 12.1$ km. An example of strong wave breaking is shown in Fig. 17 for RF09 leg 9 over Mt. Cook. The large-scale mountain wave brings the flow nearly to rest (i.e., from $U = 25$ to $3\,m\,s^{-1}$) and in this slow region small-scale turbulence is found. The wave breaking occurs in a layer above the extratropical jet within a zone of reversed wind shear similar to that seen in T-REX (e.g., Doyle et al. 2011). The dominant w scale is about 500 m (spectrum not shown), in agreement with Whiteway et al. (2003). The corrected static pressure reaches a maximum in the stagnant zone as expected in decelerated flow. At the downstream end of the turbulent zone, the air temperature jumps downward from −52° to −62°C associated with a 5-km-wide steep upward jet with $w = 3\,m\,s^{-1}$. The slow flow, high pressure, sharp cold updraft, and turbulence suggest wave overturning.

8. Comparison with previous mountain wave projects

To put the New Zealand DEEPWAVE results in a broader context, we recall a few strong mountain wave events from the literature describing low-stratosphere aircraft surveys (Table 5). We restrict ourselves to large compact mountain ranges including the Rocky Mountain Front Range (Lilly and Kennedy 1973), Pyrenees (Hoinka 1984), and Sierras (Smith et al. 2008). Each of these ridges rises 2 or 3 km above the adjacent level. The famous 11 January 1972 Boulder windstorm (Lilly 1978) cannot be compared here as it had no complete 12-km

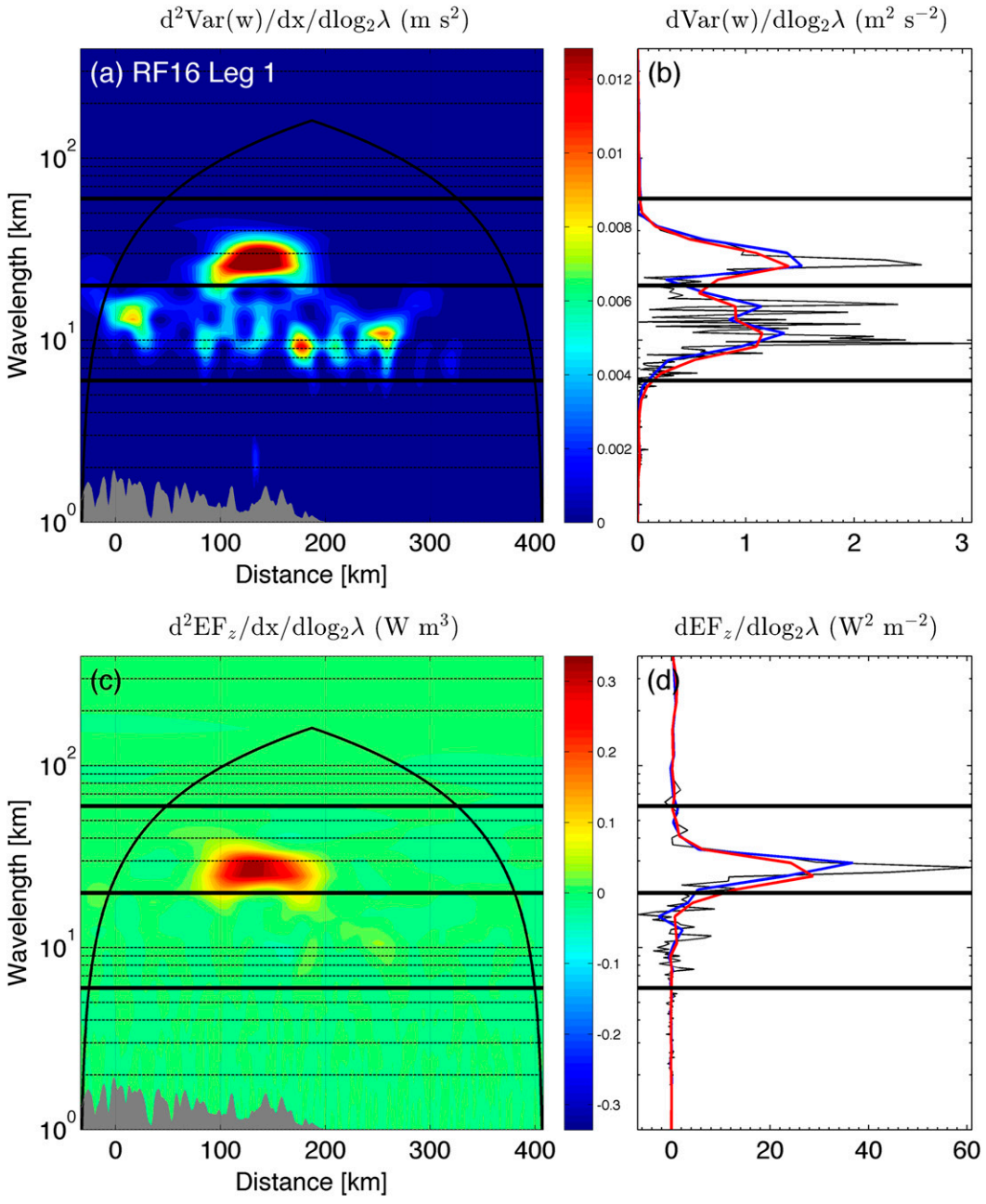

FIG. 13. As in Fig. 11, but for the extreme case of RF16 leg 1 with $EF_z = 22\,W\,m^{-2}$.

aircraft leg and the lower legs were contaminated by intense turbulent fluxes associated with plunging flow.

These earlier projects reported only single-component momentum fluxes, usually as leg averages, in units of pascals (i.e., $N\,m^{-2}$). If the wave field is compact, this value may be inversely related to the leg length, providing a poor basis for comparison. For this reason, in Table 5, we also estimate a leg-sum momentum flux in units of kilonewtons per meter. Another problem is that many earlier projects did not estimate dominant wavelengths for fluxes or w power, so in Table 5 we have estimated wave scales from their figures.

In Table 5, we see that the maximum momentum fluxes and wave scales are comparable in all four projects. The DEEPWAVE project goes beyond earlier projects in regard to comparison of ocean versus terrain regions, flux error estimates, vertical and horizontal energy flux computations, statistical evidence of scale "downshifting," rapid flux variation, short fluxless waves, and occasional wave overturning and breaking.

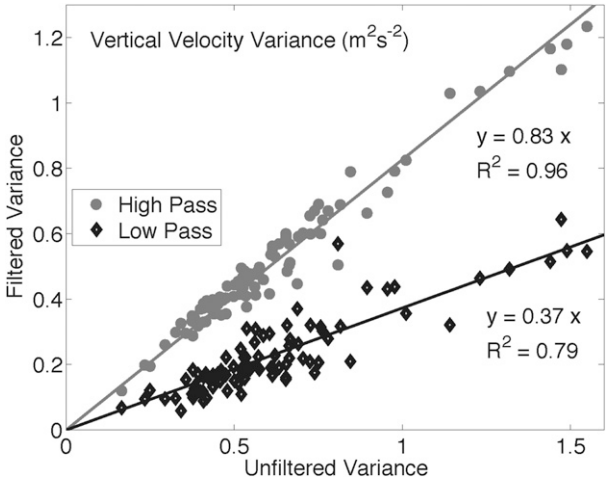

FIG. 14. Vertical velocity variance ($m^2 s^{-2}$) for all New Zealand legs using a filter ($N = 45$, $D = 10.8$ km, $\lambda_C = 24$ km) to separate short (i.e., high pass) and intermediate (i.e., low pass) wavelengths (Table 4).

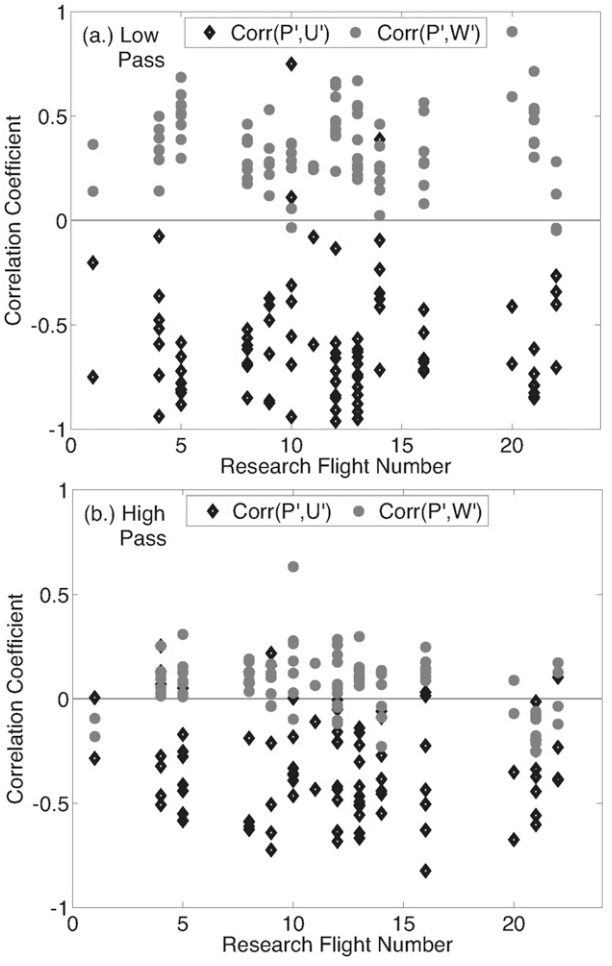

FIG. 15. (a) Velocity–pressure correlation coefficient [(14)] using a filter ($N = 45$, $D = 10.8$ km, $\lambda_C = 24$ km) to separate short and intermediate waves (Table 4). Abscissa is the research flight number for New Zealand legs only. Correlations CC(p', w') and CC(p', u') indicate the efficiency of vertical and horizontal energy propagation, respectively. (a) Low-pass signal and (b) high-pass signal. Note that the short (i.e., high pass) waves propagate upwind but not vertically.

9. Conclusions

This exploratory statistical analysis of the extensive DEEPWAVE GV dataset has two primary objectives: first, estimating the quality and uncertainty in wave flux estimates and second, describing the scale and physical character of gravity waves over New Zealand.

a. Data quality and flux uncertainty

The DEEPWAVE GV gravity wave surveys benefited from recent improved calibrations of aircraft wind and pressure sensors (Cooper et al. 2014). We also had redundant sensors for wind, pressure, and geometric altitude. The comparison of our "primary" and "secondary" sensors helped in defining sensor and flux errors. Our flux uncertainties are 0.03 Pa for momentum flux and 0.4 and 2 W m^{-2} for vertical and horizontal energy fluxes, respectively (Table 3). Horizontal energy flux is the largest and the most accurately measured flux with a relative error less than 5%. These uncertainties are measurement errors and do not include sampling errors that are likely to be large in aircraft penetration of complex wave fields.

Further tests of data quality involved the use of two laws of air motion: linearized momentum and the geostrophic law. The linearized momentum equation describes an inverse relationship between pressure and wind speed perturbations. It underlies the Eliassen–Palm (Eliassen and Palm 1960) relationship between wave energy and momentum flux shown in (10) and Fig. 5c. DEEPWAVE achieved a significantly improved verification of this law, in part by removing the geostrophic part of the pressure gradient in the energy flux calculation. An independent check on our ability to measure atmospheric pressure is the good comparison with the geostrophic pressure gradient (Fig. 2).

b. Gravity wave characteristics

The role of mountains in gravity wave generation was well established in DEEPWAVE by comparing fluxes on 97 New Zealand mountain legs with 150 ocean legs (Fig. 4). With few exceptions, the ocean leg fluxes were below the detection thresholds from Table 3. Most of the exceptions were legs over small islands. While several DEEPWAVE ocean flights targeted forecasted waves in the stratosphere from fronts or convection, none of these flights found fluxes clearly exceeding our detection

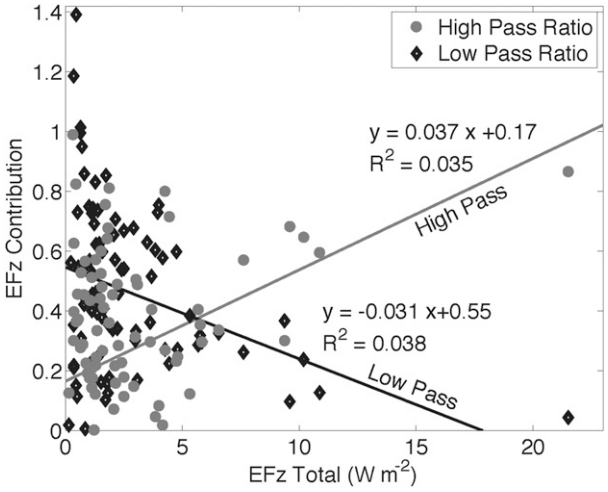

FIG. 16. The fractional contribution of long and intermediate waves to the total EF_z for 93 New Zealand legs. The fluxes are partitioned with a high- and low-pass filter with $N = 120$, $D = 28.8$ km, and $\lambda_C = 64$ km. Ordinate is the ratio of the filtered to unfiltered EF_z. Abscissa is the total EF_z from unfiltered data. The long waves (diamonds) dominate most legs but the intermediate waves (circles) dominate the strong events with $EF_z > 4\,W\,m^{-2}$. The extreme case with total $EF_z = 22\,W\,m^{-2}$ (RF16 leg 1) is dominated by short waves.

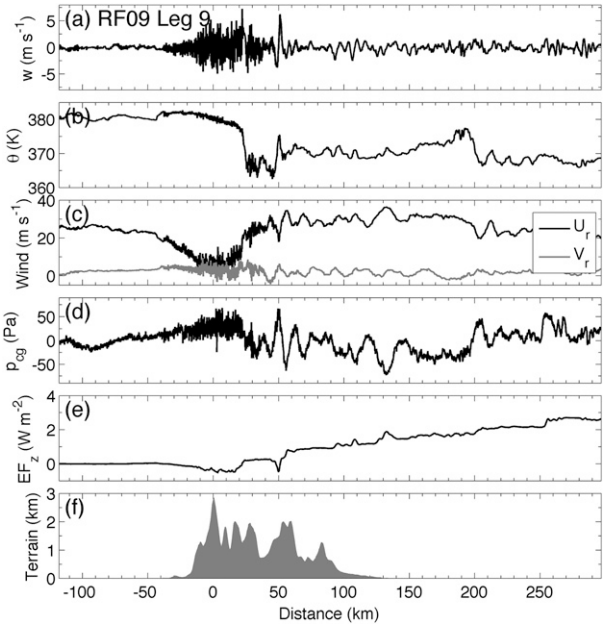

FIG. 17. Aircraft transect (as in Figs. 10 and 12), but for the wave breaking case (RF9 leg 9). This leg shows flow deceleration and turbulent wave breaking over Mt. Cook.

threshold. This result does not rule out the future identification of nonorographic (e.g., convective or frontal) wave generation but it puts bounds on their magnitude and frequency of occurrence in the low stratosphere at $z = 12.1$ km.

Our airborne remote sensing instruments (e.g., lidars and passive infrared sensors) frequently found waves in the upper stratosphere and mesosphere on ocean legs (Fritts et al. 2016). These middle-atmosphere waves may have been generated in the troposphere at a different location or time, or they may have been generated above the aircraft altitude. It is also possible that small-amplitude "subdetection" waves at flight level may have amplified aloft owing to the decreasing air density. This result reminds us of the difficulty of judging the relative global importance of large-amplitude waves over small areas of high terrain and barely detectable waves over the vast oceans.

A recurring question in the present analysis is whether the observed waves are steady. In section 3b, we showed that the steady-state relationship between EF_z and momentum flux is well satisfied. In section 3d, we found that the horizontal EF is qualitatively consistent with steady mountain wave theory. In section 3e, we found that the fluxes can vary significantly between legs 45 min apart. In section 5, we assumed steady conditions to compute vertical displacement but noted some difference from leg to leg. To resolve these contradictions we mention a few relevant time scales. The advection time of air parcels through a distance D is $T = D/U$ where U is the wind speed—say $30\,m\,s^{-1}$. For a 20-km wave $T = 670$ s ~ 11 min. The time for wave energy to propagate from the surface to flight level (H) is $T = H/C_{GZ}$, where the vertical group velocity for quasi-steady waves is typically $C_{GZ} = U^2k/N \sim 27\,m\,s^{-1}$, so $T = 12\,000/27 = 444$ s $= 7$ min. These values suggest that a wave varying over an hour could still appear steady in terms of the dominance of the advective frequency and the response to surface forcing. Other aspects of wave unsteadiness are discussed by Chen et al. (2005).

TABLE 5. Flux-carrying waves from earlier wave surveys in the low stratosphere.

Project	Location	Year	MF_x (Pa)	Leg length (km)	MF_x (kN m^{-1})	Wavelength (km)	Aircraft
Colorado Lee Wave	Front range	1970	−0.4	300	120	50	RB-57
PYREX	Pyrenees	1990	−0.2	300	60	40	DLR-Falcon
T-REX	Sierras	2006	−1	150	150	30	NSF/NCAR GV
DEEPWAVE	Southern Alps	2014	−0.5	350	175	30–120	NSF/NCAR GV

Over the New Zealand mountains, observed long and intermediate waves had the expected attributes of steady mountain waves: positive vertical energy flux (EF_z), negative zonal momentum flux (MF_x), and upwind horizontal energy flux (EF_x, EF_y). The extreme leg-averaged values of these fluxes were $EF_z = 22\,W\,m^{-2}$, $MF_x = -0.55\,Pa$, and $EF_x = -150\,W\,m^{-2}$, respectively. In general, these fluxes increased with wind speed across the mountains, but in a chaotic way (Fig. 6). On the strongest wind days [e.g., RF16 with $U(z = 4\,km) > 25\,m\,s^{-1}$], the aircraft observed fluxes fluctuated rapidly in time, perhaps owing to an instability of some sort. Unlike the T-REX project over the Sierras in 2006, no downward-propagating waves were seen (Smith et al. 2008).

The GV flight-level measurements of air motion, temperature, and pressure over New Zealand found scales ranging from a few tens of meters to 350 km. To disentangle this complex mix of scales, we defined four categories of wavelengths: long (60–150 km), intermediate (20–60 km), short (6–20 km), and turbulence (<2 km) (see Table 4). In most cases, the flux-carrying waves fell in the long and intermediate categories. This result suggests that future observations, theory, and modeling of gravity wave momentum fluxes should focus on the wavelength range from 20 to 150 km.

During strong wave events ($EF_z > 4\,W\,m^{-2}$), the dominant wavelength shortened markedly and fell into our intermediate category (i.e., 20–60 km). We describe this process as scale ''downshifting.'' The larger fluxes are carried not just by stronger waves but by shorter waves. While the rapid change in energy and momentum flux (section 3e) and the scale downshifting (section 6c) may require a nonlinear theory, a simple hypothesis is that the low-level flow may shift quickly from ''terrain following'' to ''envelope following.'' By envelope following we mean that the air flows over the higher ridges without descending into the valleys. The occasional inability of airflow to flush out cold valley air is well documented (e.g., Lareau et al. 2013; Vosper et al. 2014). An idealized example of downshifting is given in appendix B using an analytical linear hydrostatic formulation. Realistic numerical simulation of this hypothesized mechanism would require a model with a boundary layer designed to respond properly to steep terrain and horizontal pressure gradients (e.g., Smith et al. 2002; Smith 2007; Doyle and Durran 2002; Zängl 2012; Lundquist et al. 2012).

Also surprising was the common occurrence of short waves (6–20 km) at flight level over New Zealand. They occur in bursts over and downwind of high terrain. These smooth quasi-periodic motions dominate the w power at flight level. With typical vertical velocity magnitudes of $2\,m\,s^{-1}$, they cause the air to oscillate vertically with peak-to-trough amplitude of about 200 m. Similar to the intermediate and long waves, they exhibit an upwind energy flux indicating that they are trying to fight against the advection of wave energy by the ambient wind. They carry little or no vertical flux of energy and momentum, however. In this characteristic, they resemble ducted lee waves often seen in the lower troposphere. If they are ducted, they may be riding on the tropopause inversion layer often seen in balloon soundings (Fig. 8) as well as dropsonde and MTP soundings not shown here. These short waves may have leaked upward into the stratosphere from rough terrain below, but it is also possible that they were generated locally in the stratosphere by a nonlinear process. Waves near the tropopause with wavelengths in the 6–12-km range have been reported before by Duck and Whiteway (2005) and Smith et al. (2008).

On four occasions, the aircraft ascended to 13 km and encountered breaking gravity waves. The wave breaking is characterized by flow stagnation, high pressure, strong cold ascent, and turbulence with 500-m eddies.

We have shown that the DEEPWAVE GV dataset is a valuable resource for the study of gravity waves in Earth's atmosphere. Our analysis herein is primarily statistical. The present work will be followed by detailed case studies including data from the DLR Falcon, balloons, dropsondes, and remote sensing data. Research issues identified in this study include scale downshifting, flux unsteadiness or oscillation, short fluxless waves dominating w power in the stratosphere, and turbulent wave breaking. An understanding of these occurrences will require detailed theoretical analysis and numerical simulation. A further challenge in DEEPWAVE is to relate wave properties found at flight level, described here, with those found in middle stratosphere and above with remote sensing instruments. Ultimately, we hope to clarify the impact of gravity waves on the general circulation.

Acknowledgments. The DEEPWAVE project was supported primarily by the U.S. National Science Foundation with Program Manager Anne-Marie Schmoltner. The grant to Yale University was NSF-AGS-1338655 and to GATS was NSF-AGS-1338648. Additional support came from Naval Research Laboratory, German DLR, and the New Zealand Met Office and NIWA. Several staff from the Earth Observing Lab at NCAR participated in the field program including the operations manager Jim Moore and Vidal Salazar and aircraft staff leader Lou Lussier. Julie Haggerty and Kelly Schick analyzed the MTP data. We acknowledge assistance from Campbell Watson, Azusa Takeishi, Christine Tsai,

Richard Turner, Mike Revell, Andy Sturman, Dominic Pautet, Alex Reinecke, Ulrich Schumann, and other members of the DEEPWAVE team. The first author also thanks the staff of GlideOmarama for his appreciation of New Zealand's rugged terrain.

APPENDIX A

Some Previous Gravity Wave Field Campaigns

- Sierra Wave Project from 1951 to 1955 (e.g., Grubišić and Lewis 2004).
- High-Altitude Clear Air Turbulence (HICAT) from 1964 to 1968 (Lilly et al. 1974).
- Colorado Lee Wave Experiment in 1970 (Lilly and Kennedy 1973).
- Wave Momentum Flux Experiment (WAMFLEX) in 1973 (Lilly et al. 1982).
- Appalachian Lee Wave Experiment in 1971 (Smith 1976).
- Alpine Experiment (ALPEX) in 1982 (e.g., Kim and Mahrt 1992).
- Airborne Arctic Stratosphere Expedition (AASE) in 1989 (Bacmeister et al. 1996).
- Pyrenees Experiment (PYREX) in 1990 (Hoinka 1984; Bougeault et al. 1997).
- Mesocale Alpine Experiment (MAP) in 1999 (e.g., Smith and Broad 2003; Doyle and Smith 2003; Smith et al. 2007).
- T-REX in 2006 (e.g., Smith et al. 2008; Doyle et al. 2011, Wroblewski et al. 2010).
- Stratosphere–Troposphere Analysis of Regional Transport 2008 (START08) (Zhang et al. 2015).
- Gravity Wave Life Cycle (GW-LCYCLE) in 2013 (Ehard et al. 2016).

APPENDIX B

Hydrostatic Wave Drag Spectra on Smooth and Rough Hills

Consider two 2D hill shapes: a smooth Gaussian

$$h(x) = h_m \exp\left[-\left(\frac{x}{d}\right)^2\right] \quad \text{for} \quad -\infty < x < \infty \tag{B1}$$

and a four-bump elevated cosine

$$h(x) = \left(\frac{h_m}{2}\right)\left[1 - \cos\left(\frac{2\pi x}{d}\right)\right] \quad \text{for} \quad -2d < x < 2d \tag{B2}$$

shown in Fig. B1 with scales $d = 40$ km and $d = 20$ km, respectively. Note the qualitative similarity between (B2) and the rugged New Zealand terrain in Figs. 9, 10, and 12. With the Fourier Transform defined as

$$\hat{h}(k) = \int_{-\infty}^{\infty} h(x)\exp(ikx)\,dx, \tag{B3}$$

the two transforms are

$$\hat{h}(k) = (h_m\sqrt{\pi}d)\exp\left(-\frac{k^2d^2}{4}\right) \quad \text{and} \tag{B4}$$

$$\hat{h}(k) = \left(\frac{h_m}{2}\right)\left\{\left[\frac{2}{k} - \frac{1}{(k_m + k)} - \frac{1}{(k_m - k)}\right]\sin(2kd)\right\}, \tag{B5}$$

respectively. In (B5), the wavelength is d and the corresponding wavenumber $k_m = 2\pi/d$. With these

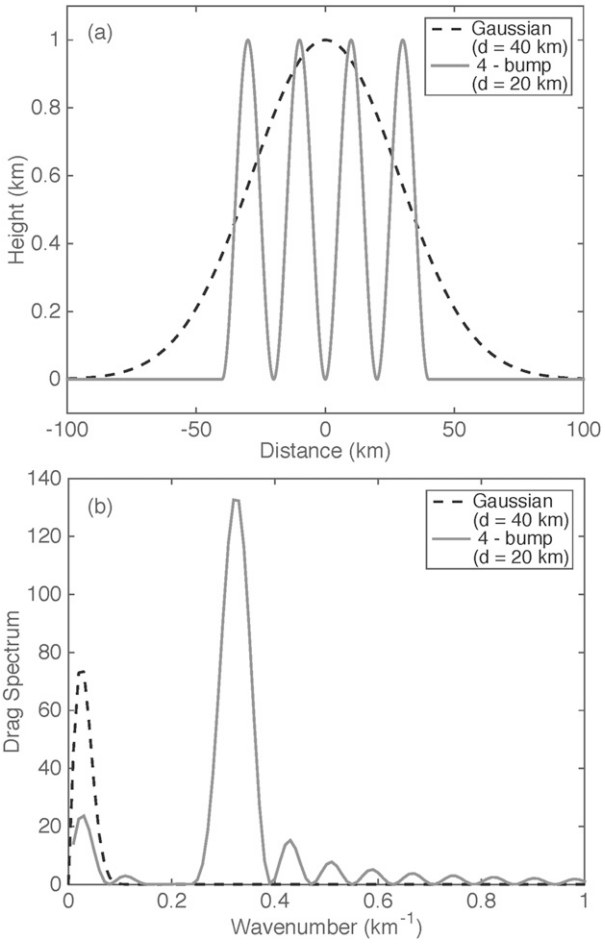

FIG. B1. Two idealized hill shapes (i.e., four bump: solid line and Gaussian: dashed line) representing terrain-following and envelope-following airflow. The two terrains [(B1) and (B2)] and (b) the two linear hydrostatic drag spectra [(B6)].

formulas, the linearized hydrostatic wave drag for an atmosphere with constant N and U can be computed using Parseval's theorem giving

$$\text{Drag} = \left(\frac{\rho NU}{2\pi}\right)\int_{-\infty}^{\infty} |k|\hat{h}(k)\hat{h}^*(k)\,dk = C_D\rho NUh_m^2, \tag{B6}$$

where we refer to the integrand as the ''drag spectrum'' (Smith 2004) shown in Fig. B1b. The two drag coefficients [(11)], proportional to the area under the curves, are $C_D = 1$ and $C_D = 3.9$, respectively. Note that the width scale d cancels out of the drag; it's the shape that matters. The rough four-bump hill shape has a drag spectrum that peaks at a much higher wavenumber than the smooth Gaussian: that is, $k_{\text{MAX}} = 0.3\,\text{km}^{-1}$ versus $k_{\text{MAX}} = 0.03\,\text{km}^{-1}$ corresponding to wavelengths of 20 versus 200 km. Other examples of rough and smooth analytical hill shapes show similar differences. This inverse relationship between wave scale and drag mimics the ''scale downshifting'' found in the Gulfstream V data. It arises here because short hydrostatic waves of the same amplitude carry more momentum per unit length.

REFERENCES

Alexander, M. J., and Coauthors, 2010: Recent developments in gravity-wave effects in climate models and the global distribution of gravity-wave momentum flux from observations and models. *Quart. J. Roy. Meteor. Soc.*, **136**, 1103–1124, doi:10.1002/qj.637.

Bacmeister, J. T., S. D. Eckermann, P. A. Newman, L. Lait, K. R. Chan, M. Loewenstein, M. H. Proffitt, and B. L. Gary, 1996: Stratospheric horizontal wavenumber of winds, potential temperature, and atmospheric tracers observed by high-altitude aircraft. *J. Geophys. Res.*, **101**, 9441–9470, doi:10.1029/95JD03835.

Birner, T., 2006: Fine-scale structure of the extratropical tropopause region. *J. Geophys. Res.*, **111**, D04104, doi:10.1029/2005JD006301.

Bougeault, P., B. Benech, P. Bessemoulin, B. Carissimo, A. Jansa Clar, J. Pelon, M. Petitdidier, and E. Richard, 1997: PYREX: A summary of findings. *Bull. Amer. Meteor. Soc.*, **78**, 637–650, doi:10.1175/1520-0477(1997)078<0637:PASOF>2.0.CO;2.

Bretherton, F. P., 1969: Momentum transfer by gravity waves. *Quart. J. Roy. Meteor. Soc.*, **95**, 213–243, doi:10.1002/qj.49709540402.

Chen, C.-C., D. R. Durran, and G. J. Hakim, 2005: Mountain-wave momentum flux in an evolving synoptic-scale flow. *J. Atmos. Sci.*, **62**, 3213–3231, doi:10.1175/JAS3543.1.

Cooper, W. A., S. M. Spuler, M. Spowart, D. H. Lenschow, and R. B. Friesen, 2014: Calibrating airborne measurements of airspeed, pressure and temperature using a Doppler laser air-motion sensor. *J. Atmos. Meas. Tech.*, **7**, 3215–3231, doi:10.5194/amt-7-3215-2014.

Doyle, J. D., and D. R. Durran, 2002: The dynamics of mountain-wave induced rotors. *J. Atmos. Sci.*, **59**, 186–201, doi:10.1175/1520-0469(2002)059<0186:TDOMWI>2.0.CO;2.

——, and R. B. Smith, 2003: Mountain waves over the Hohe Tauern: Influence of upstream diabatic effects. *Quart. J. Roy. Meteor. Soc.*, **129**, 799–823, doi:10.1256/qj.01.205.

——, Q. Jiang, R. B. Smith, and V. Grubišić, 2011: Three-dimensional characteristics of stratospheric mountain waves during T-REX. *Mon. Wea. Rev.*, **139**, 3–23, doi:10.1175/2010MWR3466.1.

Duck, T. J., and J. A. Whiteway, 2005: The spectrum of waves and turbulence at the tropopause. *Geophys. Res. Lett.*, **32**, L07801, doi:10.1029/2004GL021189.

Ehard, B., P. Achtert, A. Dörnbrack, S. Gisinger, J. Gumbel, M. Khaplanov, M. Rapp, and J. Wagner, 2016: Combination of lidar and model data for studying deep gravity wave propagation. *Mon. Wea. Rev.*, **144**, 77–98, doi:10.1175/MWR-D-14-00405.1.

Eliassen, A., and E. Palm, 1960: On the transfer of energy in stationary mountain waves. *Geofys. Publ.*, **22** (3), 1–23.

Fritts, D. C., and G. D. Nastrom, 1992: Sources of mesoscale variability of gravity waves. Part II: Frontal, convective, and jet stream excitation. *J. Atmos. Sci.*, **49**, 111–127, doi:10.1175/1520-0469(1992)049<0111:SOMVOG>2.0.CO;2.

——, and Coauthors, 2016: The Deep Propagating Gravity Wave Experiment (DEEPWAVE): An airborne and ground-based exploration of gravity wave propagation and effects from their sources throughout the lower and middle atmosphere. *Bull. Amer. Meteor. Soc.*, **97**, 425–453, doi:10.1175/BAMS-D-14-00269.1.

Geller, M. A., and Coauthors, 2013: A comparison between gravity wave momentum fluxes in observations and climate models. *J. Climate*, **26**, 6383–6405, doi:10.1175/JCLI-D-12-00545.1.

Gettelman, A., and T. Wang, 2015: Structural diagnostics of the tropopause inversion layer and its evolution. *J. Geophys. Res. Atmos.*, **120**, 46–62, doi:10.1002/2014JD021846.

Gill, A., 1982: *Atmosphere–Ocean Dynamics*. Academic Press, 662 pp.

Gossard, E. E., and W. H. Hooke, 1975: *Waves in the Atmosphere*. Developments in Atmospheric Science, Vol. 2, Elsevier, 472 pp.

Grubišić, V., and J. Lewis, 2004: Sierra Wave Project revisited: 50 years later. *Bull. Amer. Meteor. Soc.*, **85**, 1127–1142, doi:10.1175/BAMS-85-8-1127.

Hoinka, K. P., 1984: Observations of a mountain wave event over the Pyrenees. *Tellus*, **36A**, 369–383, doi:10.1111/j.1600-0870.1984.tb00255.x.

Holton, J. R., 1982: The role of gravity wave induced drag and diffusion in the momentum budget of the mesosphere. *J. Atmos. Sci.*, **39**, 791–799, doi:10.1175/1520-0469(1982)039<0791:TROGWI>2.0.CO;2.

Kim, J., and L. Mahrt, 1992: Momentum transport by gravity waves. *J. Atmos. Sci.*, **49**, 735–748, doi:10.1175/1520-0469(1992)049<0735:MTBGW>2.0.CO;2.

Kruse, C. G., and R. B. Smith, 2015: Gravity wave diagnostics and characteristics in mesoscale fields. *J. Atmos. Sci.*, **72**, 4372–4392, doi:10.1175/JAS-D-15-0079.1.

Lareau, N. P., E. Crosman, C. D. Whiteman, J. D. Horel, S. W. Hoch, W. O. J. Brown, and T. W. Horst, 2013: The Persistent Cold-Air Pool Study. *Bull. Amer. Meteor. Soc.*, **94**, 51–63, doi:10.1175/BAMS-D-11-00255.1.

Lilly, D. K., 1978: A severe downslope windstorm and aircraft turbulence event induced by a mountain wave. *J. Atmos. Sci.*, **35**, 59–77, doi:10.1175/1520-0469(1978)035<0059:ASDWAA>2.0.CO;2.

——, and P. J. Kennedy, 1973: Observations of a stationary mountain wave and its associated momentum flux and energy dissipation. *J. Atmos. Sci.*, **30**, 1135–1152, doi:10.1175/1520-0469(1973)030<1135:OOASMW>2.0.CO;2.

——, D. E. Waco, and S. I. Adelfang, 1974: Stratospheric mixing estimated from high-altitude turbulence measurements. *J. Applied Meteor. Climatol.*, **13**, 488–493, doi:10.1175/1520-0450(1974)013<0488:SMEFHA>2.0.CO;2.

——, J. M. Nicholls, P. J. Kennedy, J. B. Klemp, and R. M. Chervin, 1982: Aircraft measurements of wave momentum flux over the Colorado Rocky Mountains. *Quart. J. Roy. Meteor. Soc.*, **108**, 625–642, doi:10.1002/qj.49710845709.

Lundquist, K. A., F. Katopodes Chow, and J. K. Lundquist, 2012: An immersed boundary method enabling large-eddy simulations of flow over complex terrain in the WRF Model. *Mon. Wea. Rev.*, **140**, 3936–3955, doi:10.1175/MWR-D-11-00311.1.

Nappo, C. J., 2012: *Atmospheric Gravity Waves*. International Geophysics Series, Vol. 102, Academic Press, 321 pp.

Parish, T. R., M. D. Burkhart, and A. R. Rodi, 2007: Determination of the horizontal pressure gradient force using global positioning system on board an instrumented aircraft. *J. Atmos. Oceanic Technol.*, **24**, 521–528, doi:10.1175/JTECH1986.1.

Queney, P., 1948: The problem of air flow over mountains: A summary of theoretical results. *Bull. Amer. Meteor. Soc.*, **29**, 16–26.

Scorer, R. S., 1949: Theory of waves in the lee of mountains. *Quart. J. Roy. Meteor. Soc.*, **75**, 41–46, doi:10.1002/qj.49707532308.

Smith, R. B., 1976: The generation of lee waves by the Blue Ridge. *J. Atmos. Sci.*, **33**, 507–519, doi:10.1175/1520-0469(1976)033<0507:TGOLWB>2.0.CO;2.

——, 1985: On severe downslope winds. *J. Atmos. Sci.*, **42**, 2597–2603, doi:10.1175/1520-0469(1985)042<2597:OSDW>2.0.CO;2.

——, 2004: Mountain meteorology and regional climates. *Atmospheric Turbulence and Mesoscale Meteorology*, E. Fedorovich, R. Rotunno, and B. Stevens, Eds., Cambridge University Press, 193–222.

——, 2007: Interacting mountain waves and boundary layers. *J. Atmos. Sci.*, **64**, 594–607, doi:10.1175/JAS3836.1.

——, S. Skubis, J. Doyle, A. Broad, N. Volkert, and C. Kiemle, 2002: Mountain waves over Mt. Blanc: The role of a stagnant boundary layer. *J. Atmos. Sci.*, **59**, 2073–2092, doi:10.1175/1520-0469(2002)059<2073:MWOMBI>2.0.CO;2.

——, J. D. Doyle, Q. Jiang, and S. A. Smith, 2007: Alpine gravity waves: Lessons from MAP regarding mountain wave generation and breaking. *Quart. J. Roy. Meteor. Soc.*, **133**, 917–936, doi:10.1002/qj.103.

——, B. K. Woods, J. Jensen, W. A. Cooper, J. D. Doyle, Q. Jiang, and V. Grubišić, 2008: Mountain waves entering the stratosphere. *J. Atmos. Sci.*, **65**, 2543–2562, doi:10.1175/2007JAS2598.1.

Smith, S. A., and A. S. Broad, 2003: Horizontal and temporal variability of mountain waves over Mt. Blanc. *Quart. J. Roy. Meteor. Soc.*, **129**, 2195–2216, doi:10.1256/qj.02.148.

Sutherland, B. R., 2010: *Internal Gravity Waves*. Cambridge University Press, 394 pp.

Vosper, S. B., and S. D. Mobbs, 1998: Momentum fluxes due to three-dimensional gravity-waves: Implications for measurements and numerical modeling. *Quart. J. Roy. Meteor. Soc.*, **124**, 2755–2767, doi:10.1002/qj.49712455211.

——, J. K. Hughes, A. P. Lock, P. F. Sheridan, A. N. Ross, B. Jemmett-Smith, and A. R. Brown, 2014: Cold-pool formation in a narrow valley. *Quart. J. Roy. Meteor. Soc.*, **140**, 699–714, doi:10.1002/qj.2160.

Whiteway, J. A., E. G. Pavelin, R. Busen, J. Hacker, and S. Vosper, 2003: Airborne measurements of gravity wave breaking at the tropopause. *Geophys. Res. Lett.*, **30**, 2070, doi:10.1029/2003GL018207.

Woods, B. K., and R. B. Smith, 2010: Energy flux and wavelet diagnostics of secondary mountain waves. *J. Atmos. Sci.*, **67**, 3721–3738, doi:10.1175/2009JAS3285.1.

Wroblewski, D. E., O. R. Coté, J. M. Hacker, and R. J. Dobosy, 2010: Velocity and temperature structure functions in the upper troposphere and lower stratosphere from high-resolution aircraft measurements. *J. Atmos. Sci.*, **67**, 1157–1170, doi:10.1175/2009JAS3108.1.

Zängl, G., 2012: Extending the numerical stability limit of terrain-following coordinate models over steep slopes. *Mon. Wea. Rev.*, **140**, 3722–3733, doi:10.1175/MWR-D-12-00049.1.

Zhang, F., J. Wei, M. Zhang, K. P. Bowman, L. L. Pan, E. Atlas, and S. C. Wofsy, 2015: Aircraft measurements of gravity waves in the upper troposphere and lower stratosphere during the START08 field experiment. *Atmos. Chem. Phys.*, **15**, 7667–7684, doi:10.5194/acp-15-7667-2015.